

Discretization form of the continuity condition at the polar axis, with application to the gyrokinetic simulation in a magnetic fusion torus

Tiannan Wu, Zihao Wang, Shaojie Wang*

Department of Engineering and Applied Physics, University of Science and Technology of China, Hefei, 230026, China

Abstract

A new computational method to solve the hyperbolic (gyrokinetic Vlasov) equation coupled to the elliptic (Poisson-like) equation at the polar axis is proposed. It is shown that the value of a scalar function at the polar axis can be predicted by its neighbouring values based on the continuity condition. This continuity condition systematically solves the pole problems including the singular factor $1/r$ in the hyperbolic equation and the inner boundary in the elliptic equation. The proposed method is applied to the global gyrokinetic simulation of the tokamak plasma with the magnetic axis included.

1. Introduction

The difficulties in numerically solving partial differential equations (PDEs) at the polar axis in polar coordinates have attracted significant interest for many years. These difficulties, which are noted as pole problems in this paper, are related to (i) terms containing the geometrical singular factor $1/r$ [1], with r the radial position, (ii) inner boundary conditions needed to be specified at $r = 0$ [2, 3], even if physically there is no boundary at the polar axis, (iii) the severe numerical error of low-order finite-difference schemes, such as the second-order central difference.

In the framework of the finite-difference method (FDM) or the pseudo-spectrum method (PSM), several computational methods have been proposed

*wangs@ustc.edu.cn

to solve the pole problems. The main idea of the PSM [4] to solve Problem (i) is to use polynomial expansions in the radial direction that satisfy the regularity condition in the Cartesian coordinates. The series in radius, such as the Bessel functions or one-sided Jacobi polynomials [5, 6], can analytically remove singular terms, and thus no additional inner boundary conditions are necessary [4]. If the radial series do not completely satisfy the continuity condition, "pole conditions" [3] are preferred to replace the PDEs at the polar axis. In the PSM, the relative high numerical error near the polar axis is possible connected with Problem (ii), which can be understood as the behaviour of the global high order polynomial interpolation near the boundary [7]. One method to solve this problem is to refine the radial grids near the polar axis [3]. Another method is to use the computational domain mapping $\mathbf{M} : (0, 1) \times (-\pi, \pi) \rightarrow (-1, 1) \times (\pi/2, \pi/2)$ on a unit disk [7], where the polar axis is not treated as the inner boundary, and thus radial grid points near the polar axis will not need to be refined.

Although the FDM is less accurate than the PSM, the treatment of pole problems in the FDM is of significant interest, due to its conveniences in handling complex geometrical configurations [1] and nonlinear computation. For Problem (i), series expansions derived from the regularity condition are used to analytically remove singular factors at the polar axis [1]. Moreover, singular terms can also be avoided by shifting the grid points in the radial direction [8] so that there is no grid point situated at the polar axis. However, the shifted radial grid points may lead to the more severe numerical error of the computation of singular terms [1] at the first point off the axis. For Problem (ii), the computational domain mapping \mathbf{M} is used to avoid the inner boundary in the FDM [1, 8], which avoids the use of the one-sided finite-difference [2]. For Problem (iii), highly accurate finite-difference schemes, such as Pade schemes [9], are used to improve the accuracy of the FDM [1]. In Pade schemes, a derivative is evaluated by the values on all grid points. The numerical error of the FDM in a high wavenumber test is considerably lowered by these schemes [9].

The pole problems are of significant interest in the global gyrokinetic (GK) simulation [10] in the tokamak fusion plasma, since the magnetic axis of the fusion torus is essentially a polar axis. To simulate the ion temperature gradient (ITG) driven mode in a fusion torus with adiabatic electrons, one has to solve the GK Vlasov-Poisson (VP) system. However, the GK VP system is very computationally expensive, which simulates the time evolution of the distribution function $F(\mathbf{Z}; t)$ and the perturbed electrostatic potential

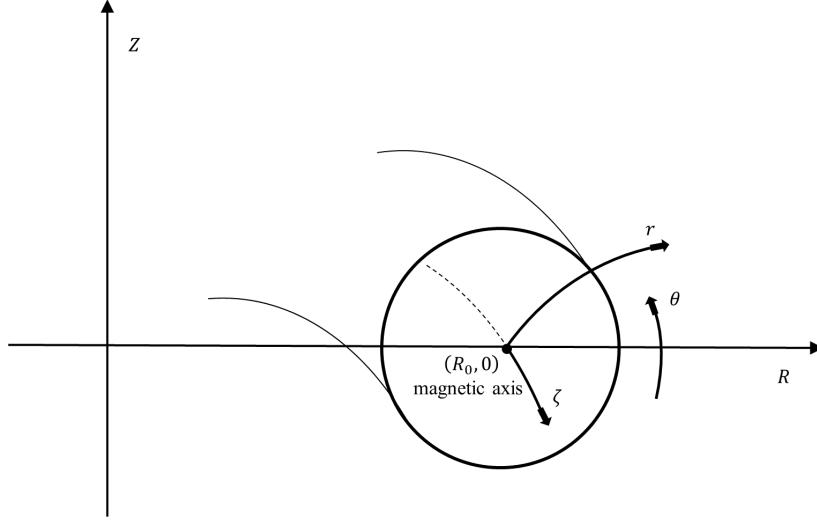


Figure 1: Magnetic flux coordinates and cylindrical coordinates.

$\delta\phi(\mathbf{X}; t)$, where $\mathbf{Z} = (\mathbf{X}, v_{\parallel}, \mu)$ are the phase space coordinates, \mathbf{X} is the position of the gyrocenter, v_{\parallel} is the parallel velocity and μ is the magnetic moment with $d\mu/dt = 0$. For higher computational efficiency, the system is usually solved in magnetic flux coordinates $\mathbf{X} = (r, \theta, \zeta)$, with $r(\psi_T) \propto \sqrt{\psi_T}$ the generalized minor radius, ψ_T the toroidal magnetic flux, θ the poloidal angle and ζ the toroidal angle. The magnetic flux coordinates discussed are graphically shown in Fig. 1. In these coordinates, the GK Vlasov equation [11] is given by

$$\frac{\partial F}{\partial t} + \dot{r} \frac{\partial F}{\partial r} + \dot{\theta} \frac{\partial F}{\partial \theta} + \dot{\zeta} \frac{\partial F}{\partial \zeta} + \dot{v}_{\parallel} \frac{\partial F}{\partial v_{\parallel}} = 0, \quad (1)$$

which is a hyperbolic equation. The GK quasi-neutrality equation [12] is given by

$$-c_1 \delta\phi + \int d^3v \left(\frac{c_1}{n_0} F \right) \langle \langle \delta\phi \rangle \rangle_{ga} - c_2 (\delta\phi - \langle \delta\phi \rangle_{FA}) = -e_i \rho_{i,gy}, \quad (2)$$

with $c_1 = \frac{e_i^2 n_0}{T_i}$, $c_2 = \frac{e^2 n_0}{T_e}$, $\langle \cdot \rangle_{FA}$ the magnetic surface averaged operator and $\langle \cdot \rangle_{ga}$ the gyro-average operator. Here n_0 is both the equilibrium ion density and the equilibrium electron density, m_i is the ion mass. T_i and e_i are the ion temperature and charge, respectively; T_e and e are the electron temperature

and charge, respectively. In the long-wavelength approximation, the GK quasi-neutrality equation becomes the Poisson-like (elliptic) equation [12]

$$\nabla \cdot (c_0 \nabla_{\perp} \delta\phi) - c_1 (\delta\phi - \langle \delta\phi \rangle_{FA}) = -e_i \rho_{i,gy}, \quad (3)$$

with $c_0 = \frac{n_0 m_i}{B_0^2}$ and B_0 the magnetic field at the magnetic axis. When approaching the magnetic axis, $r \rightarrow 0$, and r can be understood as the usual minor radius. On a minor cross section, the transformation from magnetic flux coordinates (r, θ) to cylindrical coordinates (R, Z) near the magnetic axis is given by

$$\begin{aligned} R - R_0 &= x = r \cos \theta, \\ Z &= y = r \sin \theta, \end{aligned} \quad (4)$$

where $(R - R_0, Z)$ are essentially the Cartesian coordinates (x, y) , and (r, θ) are essentially the polar coordinates. So the difficulties in the GK simulation at the magnetic axis are essentially the pole problems at the polar axis. When Eq. (3) is numerically solved with $r \rightarrow 0$, $\theta \rightarrow \infty$ is a singular term. This is Problem (i) in the GK Vlasov (hyperbolic) equation. The inner boundary at the magnetic axis in Eq. (3) is Problem (ii) in the Poisson (elliptic) equation. To include the magnetic axis in the GK simulation, we are forced to solve these problems.

In previous GK simulations, the magnetic axis is usually excluded from the simulation domain in global GK simulations [13, 14, 15]. Recently, several GK codes, such as ORB5 [16], GT5D [17] and GKNET [18], are updated to include the magnetic axis. To avoid Problem (i) in the GK Vlasov equation, cylindrical coordinates are used to avoid computing the singular terms in these codes [16, 17, 18]. However, abandoning the use of magnetic flux coordinates leads to a lower computational efficiency [16]. For Problem (ii), one of the methods is to use a numerical inner boundary condition. Different kinds of inner boundary conditions at the magnetic axis are applied in GK codes. A regular condition $\delta\phi(r = 0, \theta, \zeta) = \delta\phi(r = 0, \theta = 0, \zeta)$ is used in ORB5 [16]; a zero boundary condition at both inner and outer boundaries is used in GTC [19]; a natural boundary condition is used in GT5D [17] at the magnetic axis.

The NLT code [20, 21] evolves the perturbed distribution function δf along the equilibrium orbit by using the characteristic line method and takes account of the perturbation effects by using the numerical Lie transform [22, 23]. Recently, the NLT code has been updated to include the magnetic

axis [24], by evolving δf at the magnetic axis in terms of the cylindrical coordinates; in solving the Poisson equation in terms of the magnetic coordinates, the inner boundary condition is avoided by using the Gauss's theorem.

In this paper, a new computational method to solve pole problems is proposed. It is found that the value of a scalar function at the polar axis is predicted by its neighbouring values based on the continuity condition. Problem (i) and Problem (ii) are systematically solved by this continuity condition. The proposed method is applied to the global GK simulation of a tokamak fusion plasma, with the magnetic axis included.

The remaining part of this paper is organized as follows. In Section 2, the discretization form of the continuity condition at the polar axis is presented. In Section 3, the application of the proposed method in GK simulation for a tokamak torus is presented. In Section 4, numerical results near the magnetic axis are presented. Finally, the conclusion is presented in Section 5

2. Discretization form of the continuity condition at the polar axis

In this section, the continuity condition at the origin in the Cartesian coordinates and in the polar coordinates is discussed, and its discretization form at the polar axis is presented.

2.1. Continuity condition at the origin in the Cartesian coordinates and in the polar coordinates

The functions to be solved in the hyperbolic equation and the elliptic equation discussed here are physically observable scalars. These equations in mathematical physics can be written in any coordinates. To proceed our discussion, we introduce a fundamental assumption.

Any physical observable scalars $g(\mathbf{P})$ are \mathcal{C}^∞ in the Euclidean space, with \mathbf{P} the space point.

This fundamental assumption shall be referred to as the "continuity condition".

Following the fundamental assumption, one finds that in the Cartesian coordinates, the function $g(x, y)$, which is of interest, is \mathcal{C}^∞ at the origin. So it can be Taylor expanded, to any desired accuracy, around the origin

$$g(x, y) = \sum_{j=0}^{\infty} \sum_{k=0}^{\infty} \frac{1}{(j+k)!} \binom{j+k}{j} a_{j,k} x^j y^k, \quad (5)$$

with $a_{j,k} = \frac{\partial^{j+k} g}{\partial^j x \partial^k y}$ and $\binom{j+k}{j} = \frac{(j+k)!}{j!k!}$.

In different coordinates, the value of a scalar quantity at the same space point should be invariant. Transforming from the Cartesian to the polar coordinates (by using Eq. (4)), one finds that Eq. (5) can be written as

$$\hat{g}(r, \theta) = \sum_{m=-\infty}^{\infty} \left(\sum_{l=0}^{\infty} A_m^{(l)} r^{2l} \right) (r^{|m|} e^{im\theta}), \quad (6)$$

where we have regrouped terms with the same poloidal Fourier number m together. The expression of the coefficient $A_m^{(l)}$ in terms of $a_{j,k}$ is not important in the following.

The series expansion shown in Eq. (6) has been obtained in the previous literature [25, 26]. Lewis [25] derived Eq. (6) from the symmetry constraint in polar coordinates and the regularity constraint in Cartesian coordinates. Eisen et al. [26] proved that Eq. (6) could be derived from the regularity condition in the Cartesian coordinates.

We point that Eq. (5) is the representation of the fundamental assumption of continuity condition in Cartesian coordinates, while Eq. (6) is its representation in the polar coordinates.

Eq. (6) can be written as $\hat{g}(r, \theta) = \sum_{m=-\infty}^{\infty} \hat{g}_m(r) e^{im\theta}$, with

$$\hat{g}_m(r) = r^{|m|} \sum_{l=0}^{\infty} A_m^{(l)} r^{2l}. \quad (7)$$

It is clearly seen from Eq. (7) that powers of r in $\hat{g}_m(r)$ are not smaller than $|m|$, and that $\hat{g}_m(r)$ is an even (odd) function when m is an even (odd) number, which is the symmetry condition [25].

2.2. Discretization form at the polar axis

The continuity condition can be used to construct the numerical solution at the polar axis without solving the PDEs directly. According to Eq. (7), only the $m = 0$ component is nonzero at the polar axis, i.e., $\hat{g}(0, \theta) = \hat{g}_0(0)$. $\hat{g}_0(0)$ can be predicted by the continuity condition. In the neighbourhood of the polar axis, one finds from Eq. (7) that

$$\hat{g}_0(r) = A_0^{(0)} + A_0^{(1)} r^2 + \dots, \quad (8)$$

where the truncation error is consistent with the error of the second-order central difference. Coefficients in Eq. (8) are calculated from the \hat{g}_0 at the grid points off the polar axis, which reads

$$\begin{cases} A_0^{(0)} + A_0^{(1)}\Delta r^2 = \hat{g}_0(\Delta r), \\ A_0^{(0)} + 4A_0^{(1)}\Delta r^2 = \hat{g}_0(2\Delta r), \end{cases} \quad (9)$$

with $\Delta r = r_b/(N_r - 1)$, r_b the outer radial boundary and N_r the number of radial grid points. The uniform radial grid points are given by $r_j = (j - 1)\Delta r$, with $j = 1, 2, \dots, N_r$. Solving Eq. (9) gives

$$\hat{g}_0(0) = A_0^{(0)} = \frac{4}{3}\hat{g}_0(\Delta r) - \frac{1}{3}\hat{g}_0(2\Delta r). \quad (10)$$

The above equation can be written in the discretization form,

$$\hat{g}(0, \theta) = \frac{4}{3} \sum_{k=1}^{N_\theta} \hat{g}(\Delta r, \theta_k) - \frac{1}{3} \sum_{k=1}^{N_\theta} \hat{g}(2\Delta r, \theta_k), \quad (11)$$

with $\theta_k = -\pi + (k - 1)\Delta\theta$, $\Delta\theta = 2\pi/N_\theta$ and N_θ the number of θ grid points.

We note that Eq. (11) is the discretization form of the continuity condition at the polar axis.

Fig. (2) shows the grid points used in Eq. (11), which indicates that the value of a scalar function at the polar axis can be predicted by its average value in the neighbouring area. Therefore, Eq. (11) can be referred to as the "mean value theorem".

In solving the elliptic (Poisson-like) equation, Eq. (11) serves as the numerical inner boundary condition. This inner boundary condition is just derived from the continuity condition without any other additional assumptions (Problem (ii)); we note that the pole is not a boundary from the viewpoint of geometry or physics. In solving the hyperbolic (GK Vlasov) equation, the scalar function to be solved for at the polar axis can be predicted by the mean value theorem, without solving the hyperbolic equation itself directly at the pole; this method avoids the numerical treatment of the $1/r$ singularity term (Problem (i)).

Problems (i) and (ii) are solved above. The factor $r^{|m|}$ in Eq. (6) indicates that the numerical error of the low-order FDM near the pole may be serious; this is Problem (iii) in numerically solving PDEs at the pole, especially when there are high m components in the system. To illustrate this problem, we

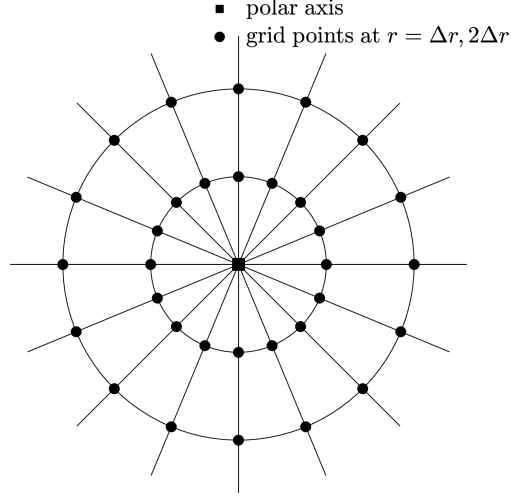


Figure 2: Predicting a scalar function at the polar axis by using the function's average value on the neighbouring points.

evaluate the numerical error in using second-order central difference method to evaluate the $\partial_r \hat{g}_m$, with $\hat{g}_m(r) = r^{|m|}$.

$$\frac{\partial \hat{g}_m}{\partial r} = \frac{(r_j + \Delta r)^{|m|} - (r_j - \Delta r)^{|m|}}{2\Delta r} \approx |m|r_j^{|m|-1} + C_{|m|}^3 \left(\frac{\Delta r}{r_j}\right)^2 r_j^{|m|-1}. \quad (12)$$

The relative error is estimated to be

$$\eta = \frac{(m-1)(m-2)}{3!} \left(\frac{\Delta r}{r_j}\right)^2, \quad (13)$$

which indicates that a larger m will dramatically increase the η . Particularly, when $m > 4$, the relative error at $r = r_2$ becomes $\eta > 1$ and the numerical error is intolerable. To solve Problem (iii), one way is to use the Pade schemes [9] to calculate the radial derivatives. However, the change from the explicit to the implicit scheme significantly reduces the computation efficiency by an order of $1/N_r$.

Here we propose that the mean value theorem can be generalized to solve Problem (iii). Eq. (7) can be written as

$$\hat{g}_m(r) = r^{|m|} (A_m^{(0)} + A_m^{(1)}r^2 + \dots), \quad (14)$$

which can be numerically evaluated at r_{j_-} and r_{j_+} ($j_+ = j_- + 1$) as

$$\begin{cases} A_m^{(0)} r_{j_-}^{|m|} + A_m^{(1)} r_{j_-}^{|m|+2} = \hat{g}_m(r_{j_-}), \\ A_m^{(0)} r_{j_+}^{|m|} + A_m^{(1)} r_{j_+}^{|m|+2} = \hat{g}_m(r_{j_+}). \end{cases} \quad (15)$$

Using $\hat{g}(r_{j_-}, \theta)$ and $\hat{g}(r_{j_+}, \theta)$, one finds $\hat{g}_m(r_-)$ and $\hat{g}_m(r_+)$; using Eq. (15), one finds the coefficients in Eq. (14), which shall be used to predict $\hat{g}(r < r_{j_-}, \theta)$. By writing $A_m^{(0)}, A_m^{(1)}$ solved in Eq. (15) as $A_m^{(0)}(j_-), A_m^{(1)}(j_-)$ respectively, one obtains

$$\hat{g}(r_j, \theta_k) = \sum_{m=-\frac{N_\theta}{2}}^{\frac{N_\theta}{2}} r_j^{|m|} [A_m^{(0)}(j_-) + A_m^{(1)}(j_-)] e^{im\theta_k}, \quad j < j_-. \quad (16)$$

This method can be understood as the "generalized mean value theorem", and the mean value theorem is the $j_- = 2$ case.

To solve Problem (iii) by using the generalized mean value theorem, we solve the PDE by using the FDM when $r \geq r_{j_-}$, and the values of the function to be solved in the domain $r < r_{j_-}$ is predicted by Eq. (14). According to Eq. (13), the numerical error of the low-order FDM decreases quickly with r increasing. Note that the truncation error of Eq. (14) quickly decreases when approaching the pole. Therefore, j_- should be chosen to be large enough to keep a small FDM error and small enough to keep a small truncation error. In practice, for a system containing $m \leq 6$ components near the pole, $j_- = 5$ can be chosen to find a good enough numerical solution, as will be discussed in Section 4.

3. Application in the gyrokinetic simulation for a tokamak torus

In a global GK code, the field-aligned coordinates $\mathbf{X} = (r(\psi_T), \alpha, \theta)$ are used to improve the computational efficiency, with $\alpha = q\theta - \zeta$ and q the safety factor. As is mentioned in Section 1, when approaching the magnetic axis, $r \rightarrow 0$, and r can be understood as the usual minor radius, so there is no difference to discuss the radial series expansions of a poloidal Fourier component shown in Eq. (7) in these coordinates. However, the θ direction is along with the field line, and the scalar function is not periodic in this direction. To implement the proposed method, a scalar function h in the field-aligned coordinates need to be transformed to the magnetic flux coordinates.

For each toroidal mode h_n , the transformation is given by

$$\bar{h}_n(r, \theta) = h_n(r, \theta)e^{inq(r)\theta}, \quad (17)$$

where $\bar{\cdot}$ represents a scalar function in the magnetic flux coordinates. \bar{h}_n is periodic in the θ direction and can be written in the Fourier series, which reads

$$\bar{h}_n(r, \theta) = \sum_{m=m_0-\frac{N\theta}{2}}^{m_0+\frac{N\theta}{2}} \bar{h}_{n,m}(r)e^{im\theta}, \quad (18)$$

with $m_0 = [nq]$; $[nq]$ is the nearest integer around nq . According to Eqs. (16) and (17), the generalized mean value theorem with a given j_- in the field-aligned coordinates is given by

$$h_n(r_j, \theta_k) = e^{-inq(r_j)\theta_k} \sum_{m=m_0-\frac{N\theta}{2}}^{m_0+\frac{N\theta}{2}} r_j^{|m|} [A_{n,m}^{(0)}(r_{j_-}) + A_{n,m}^{(1)}(r_{j_-})r_j^2] e^{im\theta_k}, \quad j < j_-, \quad (19)$$

where coefficients $A_{n,m}^{(0)}(r_{j_-}), A_{n,m}^{(1)}(r_{j_-})$ are calculated from Eq. (15) by replacing $\hat{g}_m(r_{j_-}), \hat{g}_m(r_{j_+})$ with $\bar{h}_{n,m}(r_{j_-}), \bar{h}_{n,m}(r_{j_+})$. h_n can be either the perturbed electrostatic potential $\delta\phi_n$ or the distribution function δf_n , since the dependence of the scalar function on the phase space coordinates will not affect our discussion.

The generalized mean value theorem in the field-align coordinates shown in Eq. (19) is applied to the global GK code NLT [20], which evolves the perturbed ion distribution function $\delta f(r, \alpha, \theta, v_{\parallel}, \mu) = F(r, \alpha, \theta, v_{\parallel}, \mu) - F_0(r, \theta, v_{\parallel}, \mu)$ along the equilibrium orbit by using the characteristic line method and takes account of the perturbation effects by using the numerical Lie transform [22, 23]. Here F_0 is the equilibrium ion distribution function set as a local Maxwellian distribution. The adiabatic electron assumption is used. The field-align coordinates have been applied to NLT [21]. The application of the generalized mean value theorem in solving the GK Vlasov equation and the GK quasi-neutrality equation in NLT will be presented in Sections 3.1 and 3.2. In Appendix A and Appendix B, a Rosenbluth–Hinton (R-H) test and a set of linear ITG simulations away from the magnetic axis are presented as benchmarks for NLT using the new numerical treatment at the magnetic axis.

3.1. Application in solving the GK Vlasov equation in NLT

In solving the GK Vlasov equation, firstly, $\delta f(r \geq r_{j-})$ is solved by using the characteristic line method and the numerical Lie transform [20, 21] in the usual way. Then $\delta f(r < r_{j-})$ is predicted by using $\delta f(r = r_{j-})$ and $\delta f(r = r_{j+})$. As is shown in Eq. (18), the range of m is dependent on n , therefore, $\delta f(r < r_{j-})$ is solved by predicting each toroidal mode $\delta f_n(r < r_{j-})$. Decomposing δf into different toroidal modes gives

$$\delta f(r, \alpha, \theta, v_{\parallel}, \mu) = \sum_{n=-\frac{N_{\alpha}}{2}}^{\frac{N_{\alpha}}{2}} \delta f_n(r, \theta, v_{\parallel}, \mu) e^{in\alpha}, \quad (20)$$

with N_{α} the number of α grid points. To calculate the coefficients used to predict $\delta f_n(r < r_{j-})$, the poloidal Fourier series expansion of each δf_n is given by

$$\delta \bar{f}_n(r, \theta, v_{\parallel}, \mu) = \sum_{m=m_0-\frac{N_{\theta}}{2}}^{m_0+\frac{N_{\theta}}{2}} \delta \bar{f}_{n,m}(r, v_{\parallel}, \mu) e^{im\theta}, \quad (21)$$

with $\delta \bar{f}_n = \delta f_n e^{inq\theta}$. According to Eq. (19), $\delta f_n(r < r_{j-})$ is predicted by

$$\delta f_n(r_j, \theta_k, v_{\parallel}, \mu) = e^{-inq(r_j)\theta_k} \sum_{m=m_0-\frac{N_{\theta}}{2}}^{m_0+\frac{N_{\theta}}{2}} r_j^{|m|} [C_{n,m}^{(0)}(r_{j-}) + C_{n,m}^{(1)}(r_{j-})r_j^2] e^{im\theta_k}, \quad (22)$$

$j < j-,$

where coefficients $C_{n,m}^{(0)}(r_{j-}), C_{n,m}^{(1)}(r_{j-})$ are calculated from Eq. (15) by replacing $\hat{g}_m(r_{j-}), \hat{g}_m(r_{j+})$ with $\delta \bar{f}_{n,m}(r_{j-}), \delta \bar{f}_{n,m}(r_{j+})$. $\delta f(r < r_{j-})$ is calculated by using Eq. (20) with $\delta f_n(r < r_{j-})$ predicted by the generalized mean value theorem.

Note that, in nonlinear simulation, the Fourier series expansions used in Eqs. (20) and (21) has already been computed in the nonlinear filtering module. Therefore, to apply the generalized mean value theorem, we just need to compute Eq. (22). Previously, NLT [24] solved δf at the magnetic axis in the cylindrical coordinates to avoid Problem (i). One of the advantages of using the generalized mean value theorem is that it provides the numerical solutions of the GK Vlasov equation and the GK quasi-neutrality equation, with the numerical errors consistent with each other.

3.2. Application in solving the GK quasi-neutrality equation in NLT

The perturbed electrostatic potential is decomposed into different toroidal modes in solving the GK quasi-neutrality equation, which reads

$$\delta\phi(r, \alpha, \theta) = \sum_{n=-\frac{N\alpha}{2}}^{\frac{N\alpha}{2}} \delta\phi_n(r, \theta)e^{in\alpha} \quad (23)$$

In the ITG simulation, the maximum m near the magnetic axis is dependent on the toroidal mode number n , since $m - nq$ is usually a small number.

For $n \neq 0$ modes, the long-wavelength approximation is not applied to the GK quasi-neutrality equation, and $\delta\phi_{n \neq 0}$ is solved by Eq. (2), which is not a PDE. For $n \neq 0$, Eq. (2) can be solved iteratively,

$$(c_1 + c_2)\delta\phi_n^{it+1} = e_i\rho_{i,gy,n} + \int d^3v \left(\frac{c_1}{n_0} F \right) \langle\langle \delta\phi_n^{it} \rangle\rangle_{ga}, \quad (24)$$

where it is the iteration number.

Although solving Eq. (24) is untroubled by Problem (ii), the generalized mean value method is used to achieve a numerical solution whose numerical error is consistent with δf_n . Firstly, the poloidal Fourier series expansion of each toroidal mode is given by

$$\delta\bar{\phi}_n(r, \theta) = \sum_{m=m_0-\frac{N\theta}{2}}^{m_0+\frac{N\theta}{2}} \delta\bar{\phi}_{n,m}(r)e^{im\theta}, \quad (25)$$

with $\delta\bar{\phi}_n = \delta\phi_n e^{inq\theta}$. Then $\delta\phi_n(r < r_{j-})$ can be predicted by

$$\delta\phi_n(r_j, \theta_k) = e^{-inq(r_j)\theta_k} \sum_{m=m_0-\frac{N\theta}{2}}^{m_0+\frac{N\theta}{2}} r_j^{|m|} [D_{n,m}^{(0)}(r_{j-}) + D_{n,m}^{(1)}(r_{j-})r_j^2] e^{im\theta_k}, \quad j < j-, \quad (26)$$

where coefficients $D_{n,m}^{(0)}(r_{j-}), D_{n,m}^{(1)}(r_{j-})$ are calculated from Eq. (15) by replacing $\hat{g}_m(r_{j-}), \hat{g}_m(r_{j+})$ with $\delta\bar{\phi}_{n,m}(r_{j-}), \delta\bar{\phi}_{n,m}(r_{j+})$.

Therefore, in solving Eq. (2) with $n \neq 0$, we compute $\delta\phi_n^{it+1}(r \geq r_{j-})$ by using Eq. (24), and predict $\delta\phi_n^{it+1}(r < r_{j-})$ by using Eq. (26).

For the $n = 0$ mode, the long-wavelength approximation is usually satisfied. Therefore, $\delta\phi_0$ is solved by Eq. (3), which is a Poisson-like equation. The mean value theorem ($j_- = 2$) is used to provide the inner boundary condition at the magnetic axis; the reason we choose $j_- = 2$ here is that there is no high m components in the $n = 6$ mode. The outer boundary condition is given by

$$\delta\phi_0^{N_r,k} = 0, \quad k = 1, 2, \dots, N_\theta, \quad (27)$$

with $\phi_0^{j,k} = \phi_0(r_j, \theta_k)$. By integrating both sides of Eq. (3) with $\int dr d\theta J_X$ and using the second-order central difference scheme, we obtain

$$\int_{V_{j,k}} dr d\theta J_X \nabla \cdot (c_0 \nabla_\perp \delta\phi_0) = \sum_{j'=j-1}^{j+1} \sum_{k'=k-1}^{k+1} \alpha_{j,k}^{j',k'} \delta\phi_0^{j',k'}, \quad (28a)$$

$$\int_{V_{j,k}} dr d\theta J_X c_1 (\delta\phi_0 - \langle \delta\phi \rangle_{FA}) = \beta_{j,k}^{j,k} \delta\phi_0^{j,k} - \sum_{k'=1}^{N_\theta} \nu_{j,k}^{j,k'} \delta\phi_0^{j,k'}, \quad (28b)$$

$$\int_{V_{j,k}} dr d\theta J_X e_i \rho_{i,gy,0} = \sigma_{j,k}^{j,k} \rho_{i,gy,0}^{j,k}, \quad (28c)$$

where J_X is the space Jacobian, $V_{j,k} = [r_j - \frac{1}{2}\Delta r, r_j + \frac{1}{2}\Delta r] \times [\theta_k - \frac{1}{2}\Delta\theta, \theta_k + \frac{1}{2}\Delta\theta]$ is the integral domain. The coefficients $\alpha_{j,k}^{j',k'}$, $\beta_{j,k}^{j,k}$, $\nu_{j,k}^{j,k'}$, $\sigma_{j,k}^{j,k}$ are shown in Appendix C. According to Eqs. (28a)-(28c), the numerical equations at grid points (r_j, θ_k) are given by

$$\sum_{j'=j-1}^{j+1} \sum_{k'=k-1}^{k+1} \alpha_{j,k}^{j',k'} \delta\phi_0^{j',k'} - \beta_{j,k}^{j,k} \delta\phi_0^{j,k} + \sum_{k'=1}^{N_\theta} \nu_{j,k}^{j,k'} \delta\phi_0^{j,k'} = -\sigma_{j,k}^{j,k} \rho_{i,gy,0}^{j,k}, \quad (29)$$

where the integer indices are given by

$$\begin{aligned} j &= 2, 3, \dots, N_r - 1 \\ k &= 1, 2, \dots, N_\theta. \end{aligned}$$

Note that Eq. (29) is not defined at the magnetic axis. To obtain a unique solution (the number of equations is equal to that of variables), the numerical equations at the magnetic axis are provided by the mean value theorem, which reads

$$\delta\phi_0^{1,k} = \frac{4}{3} \sum_{k'=1}^{N_\theta} \delta\phi_0^{2,k'} - \frac{1}{3} \sum_{k'=1}^{N_\theta} \delta\phi_0^{3,k'}, \quad k = 1, 2, \dots, N_\theta. \quad (30)$$

By combining Eqs. (27), (29) and (30), we obtain full numerical equations to solve $\delta\phi_0$. Therefore, Eq. (30) can be understood as an inner boundary condition.

4. NLT simulation results including the magnetic axis

In this section, numerical results of the R-H test and the linear ITG simulation near the magnetic axis are presented for verification. Firstly, the $n = 0$ R-H test with $j_- = 2$ is presented. Then the GK simulation result of the $n > 0$ ITG mode with different j_- are presented.

4.1. R-H test

According to Ref. [27], an initial perturbed temperature will drive the electrostatic potential that balances it. This provides a convenient test for the radial force balance equation, which reads

$$\delta E_r + \delta u_\theta B_T - \delta u_\zeta B_P - \frac{\delta p_i'}{n_0 e_i} = 0, \quad (31)$$

with δE_r the perturbed radial electric field, δu_θ the perturbed poloidal flow, δu_ζ the perturbed toroidal flow, B_P the poloidal magnetic field, B_T the toroidal magnetic field, $\delta p_i = n_0 \delta T_i$ and δT_i the perturbed temperature. Here the prime represents the radial derivative. δu_ζ , δE_r and δp_i are directly given by the simulation results, while the δu_θ is calculated from Eq. (31).

The simulation parameters are set as: $B_0 = 2.00\text{T}$, the major radius $R_0 = 1.65\text{m}$, the minor radius $a = 0.40\text{m}$. To avoid profile effects, the test is carried out in the radial homogeneous plasma, with equilibrium profiles $T_{0i} = 1\text{keV}$, $\tau_e \equiv T_{0e}/T_{0i} = 1$, $n_0 = 10^{19}\text{m}^{-3}$, $q = 1.2$. The initial perturbed ion distribution function is given by

$$\delta f = \left(\frac{w}{T_{0i}} - \frac{3}{2} \right) \frac{\delta T_i}{T_{0i}} F_0, \quad (32)$$

with w the kinetic energy. Eq. (32) gives the initial source as an ion heating impulse without density and parallel momentum input. The initial perturbed temperature is set as

$$\frac{\delta T_i(r)}{T_{0i}} = 1.7 \times 10^{-3} \exp\left(-\frac{r^2}{\Delta_{\delta T}^2}\right), \quad (33)$$

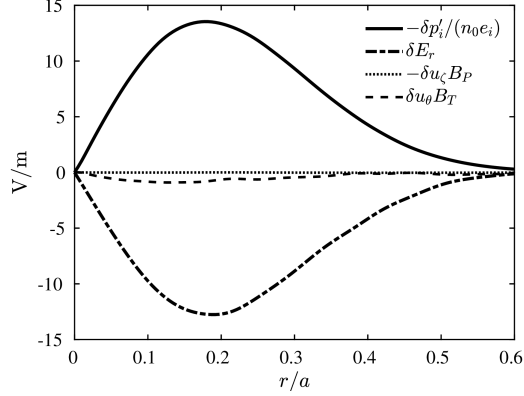


Figure 3: Different terms in the radial force balance equation.

with $\Delta_{\delta T} = 0.25a$. The $\Delta_{\delta T}$ is large enough to make the radial structure of δT_i wider than the banana width of a trapped particle whose velocity approaching v_{ti} near the magnetic axis. Although T_{0i} is radial homogeneous, v_{ti} is defined as $v_{ti} = \sqrt{2T_{0i}(r_0)/m_i}$, with $r_0 = 0$. The simulation results are shown in Fig. 3. It can be seen that the pressure gradient is well balanced with the radial electric field.

4.2. Linear ITG simulation

The ITG mode tends to be more stable near the magnetic axis where the magnetic shear, $\hat{s} = \frac{q}{r} \frac{dq}{dr}$, is weaker. So, these tests are carried out with the internal transport barrier (ITB) like profiles for a relative high ITG growth rate near the magnetic axis. The main parameter are set as: $B_0 = 2.10\text{T}$, $R_0 = 1.67\text{m}$, $a = 0.67\text{m}$. Equilibrium profiles are based on the ITB data in DIII-D [28]. They are set as

$$q(r) = 1.10 + 7.79 \left(\frac{r}{a}\right)^2 - 17.71 \left(\frac{r}{a}\right)^3 + 13.46 \left(\frac{r}{a}\right)^4, \quad (34a)$$

$$n_{0i}(r) = 1.25 - 1.25 \left(\frac{r}{a}\right)^2 + 0.50 \left(\frac{r}{a}\right)^3, \quad (34b)$$

$$T_{0i}(r) = -\frac{1}{2} \tanh\left(\frac{r^2 - r_m^2}{\Delta_T^2}\right) + 1, \quad (34c)$$

with $\Delta_T = 0.15a$, $r_m = 10^{-4}a$, $T_{0i}(r_0) = 3\text{keV}$ and $n_{0i}(r_0) = 2 \times 10^{19}\text{m}^{-3}$. Details of equilibrium profiles are shown in Fig. 4. Moreover, an equilibrium radial electric field E_{0r} that balances the equilibrium pressure gradient is

applied. The simulation domain are $r/a \in [0, 0.9]$, $\theta \in [-\pi, \pi]$, $\alpha \in [0, 2\pi]$, $v_{\parallel}/v_{ti} \in [3, 3]$, $\mu B_0/T_{0i}(r_0) = [0, 9]$. Grid numbers are $(N_r, N_{\alpha}, N_{\theta}, N_{v_{\parallel}}, N_{\mu}) = (200, 142, 16, 64, 16)$. μ is discretized according to the Gauss-Legendre formula, while the other variables are discretized uniformly.

The mode structure of the toroidal mode $n = 6$, which is one of the most unstable modes, on a minor cross section is shown in Fig. 5. It is a typical toroidal mode structure that balloons on the weak field side. On the strong field side, the balloon structure disappears and the amplitude of the mode is much weaker.

The eigenfunctions of the $m/n = 6/6$ harmonics $|\delta\phi_{6,6}|$ for different j_- near the magnetic axis are shown in Fig. 6. For $j_- = 2, 3, 4, 5$, $|\delta\phi_{6,6}|/r^6$ are convergent. The $|\delta\phi_{6,6}|/r^6$ for $j_- = 2, 3$ are not as good as those for $j_- = 4, 5$, which is consistent with the numerical relative error η of the second-order central difference at j_- shown in Table 1; η for $j_- = 2, 3$ are much larger than those for $j_- = 4, 5$. However, the difference of $|\delta\phi_{6,6}|$ for different j_- is not observable, since they are close to 0 when approaching the magnetic axis; this can also be seen from P_{j_-} shown in Table 1. For $j_- = 2, 3$, $|\delta\phi_{6,6}(r_{j_-})|$ is smaller than $|\delta\phi_{6,6}(r_{10})|$ by an order of 5×10^{-4} . The linear growth rates and real frequencies for different j_- shown in Table 1 are almost the same, which is due to the reason that $|\delta\phi_{6,6}|$ are consistent with each other. This indicates that to have a small error of $\delta\phi_{n,m}/r^{|m|}$ is a too strict requirement.

Clearly, to solve Problems (i) and (ii), one can use the mean value theorem [Eq. (11)]. The generalized mean value theorem [Eq. (16)] can be used to solve Problem (iii); however, according to the above discussions, even with $j_- = 2$, which corresponds to use the mean value theorem, the eigenvalue can be correctly computed, since the eigenfunction is nearly zero when approaching the magnetic axis. This suggests that to solve Problem (iii) is a too strict requirement. Therefore, one concludes that the mean value theorem is good enough in practical applications.

5. Conclusion

We have proposed a new computational method to solve the hyperbolic (such as the GK Vlasov) equation coupled to the elliptic (such as the Poisson-like) equation with the polar axis included. We have proved the mean value theorem, which indicates that the value of a scalar function at the polar axis can be predicted by the average of its neighbouring values, based on the continuity condition. This mean value theorem [Eq. (11)], which is understood

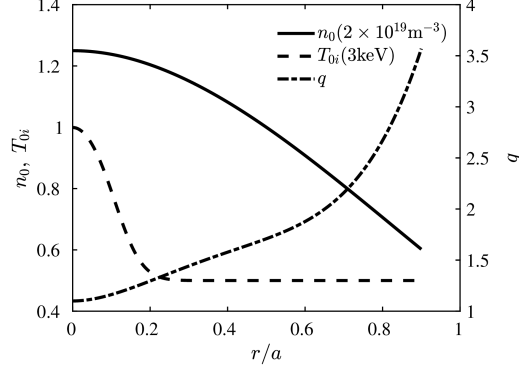


Figure 4: Equilibrium profiles used in the linear ITG simulation near the magnetic axis.

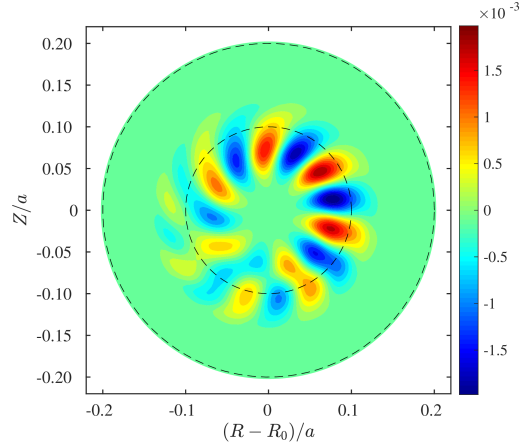


Figure 5: Mode structure of $\delta\phi$ with $n = 6$.

j_-	$\gamma (R_0/v_{ti})$	$\omega (R_0/v_{ti})$	η at r_{j_-}	P_{j_-}
2	0.219	1.816	333.3%	6.6×10^{-4}
3	0.219	1.816	83.3%	5.0×10^{-4}
4	0.219	1.816	37.0%	3.9×10^{-3}
5	0.219	1.801	20.8%	1.9×10^{-2}

Table 1: Linear growth rates, real frequencies, the numerical relative error η of the second-order central difference method at r_{j_-} , and $P_{j_-} = \delta\phi_{6,6}(r_{j_-})/\delta\phi_{6,6}(r_{10})$, for different j_- .

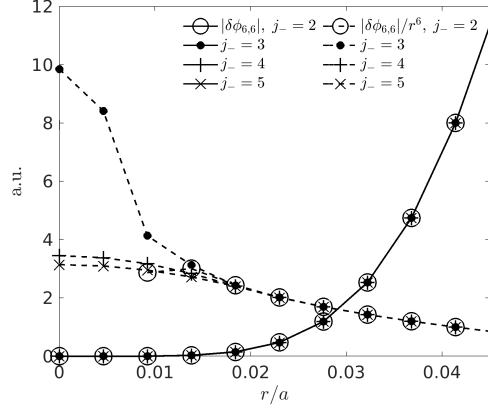


Figure 6: Eigenfunctions computed. Solid lines: $|\delta\phi_{6,6}|$; dashed lines: $|\delta\phi_{6,6}|/r^6$. $|\delta\phi_{6,6}|/r^6$ at r_1 and r_2 for $j_- = 2$ are 466.6 and 349.4, which are not plotted here.

as the discretization form of the continuity condition, systematically solves the pole problems including the problem of singular factor $1/r$ in the hyperbolic equation and the problem of inner boundary condition in the elliptic equation. Moreover, the severe numerical error of low-order finite-difference schemes near the polar axis can be solved by using the generalized mean value theorem; however, we found that the mean value theorem is good enough in practical computation, since it can correctly compute the eigenvalue, due to the fact that the eigenfunction of high m mode quickly goes to zero when approaching the polar axis.

The proposed method is applied in the global GK simulation of fusion plasmas in a tokamak torus, with the magnetic axis included. In the $n = 0$ R-H test, an initial perturbed temperature drives the electrostatic potential that balances it, which is consistent with the theoretical prediction. In the $n = 6$ linear ITG simulation, convergent eigenvalue and eigenfunction are obtained.

Although the application in the GK simulation is only discussed here for the NLT code, which is base on the numerical Lie-transform, the proposed method can also be applied in an Eulerian GK code or a particle-in-cell GK code.

Acknowledgement

This work was supported by the National MCF Energy R&D Program of China under Grant No. 2019YFE03060000, and the National Natural Science Foundation of China under Grant No. 12075240.

Appendix A. R-H test away from the magnetic axis

The R-H test of NLT has been performed in Ref. [20, 24]. In this section, a R-H test away from the magnetic axis is performed as a benchmark for the NLT using the new computational method to treat the magnetic axis. Parameters are set as following: magnetic field at the axis $B_0 = 1.50\text{T}$, major radius $R_0 = 1.25\text{m}$, minor radius $a = 0.45\text{m}$. To avoid the phase mixing effect [29], the test is carried out in radial homogeneous plasma, with equilibrium profiles $q = 1.2$, $T_{0i} = 0.15\text{keV}$, $\tau_e \equiv T_{0e}/T_{0i} = 1$. The initial perturbation is given in the form of a radial perturbed density

$$\frac{\delta n_i(r)}{n_0(r)} = \begin{cases} 10^{-5} \sin\left(\frac{r-r_a}{r_b-r_a}\right), & r \in [r_a, r_b] \\ 0, & \text{else} \end{cases} \quad (\text{A.1})$$

with δn_i the perturbed density, $r_a = 0.4a$, $r_b = 0.6a$. The radial simulation domain is $[0, 0.85a]$, which particularly includes the magnetic axis.

By taking account of the geodesic acoustic mode (GAM) oscillations, the collisionless damping and the residual flow [30], the $m = n = 0$ component of perturbed radial electric field is expected to behave as

$$\frac{\delta E_r(t)}{\delta E_r(0)} = R_F + (1 - R_F)e^{-\gamma_g t} \cos(\omega_g t) \quad (\text{A.2})$$

where $R_F = 1/(1 + 1.6q^2/\sqrt{\epsilon})$ is the residual flow, $\epsilon = r/R_0$ is inverse aspect-ratio, ω_g and γ_g are theoretical frequency and damping rate [31, 32], respectively. Fig. A.7 shows the time evolution of perturbed radial electric field at $r_0 = 0.5a$. The normalized unit of speed is defined as $v_{ti} = \sqrt{(2T_{0i}(r_0)/m_i)}$. The oscillation frequency, collisionless damping rate and residual flow all agree with the theoretical values.

Appendix B. Linear ITG simulations away from the magnetic axis

The linear ITG tests of NLT have been performed in Ref. [20, 24]. In this section, a set of linear ITG mode tests are performed to benchmark the NLT,

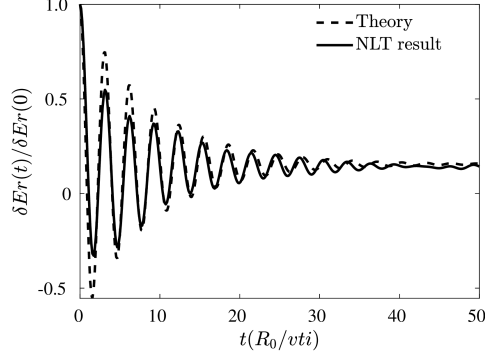


Figure A.7: Time evolution of perturbed radial electric field at r_0

which uses the new computational method to treat the magnetic axis, against another global GK code. These tests are carried out with the Cyclone Base Case (CBC) [33] parameters: $B_0 = 1.90\text{T}$, $R_0 = 1.67\text{m}$, $a = 0.60\text{m}$. The q profile is set as

$$q(r) = 0.854 + 2.4045 \left(\frac{r}{a}\right)^2 \quad (\text{B.1})$$

with $q_0 \equiv q(r_0) = 1.455$, $r_0 = 0.5$. The initial ion temperature and density profile are set as

$$\hat{A}(r) = \frac{A(r)}{A(r_0)} = \exp \left[-\kappa_A \frac{a}{R_0} \Delta_A \tanh \left(\frac{r - r_0}{a} \right) \right], \quad (\text{B.2})$$

where A can be chosen as either T_{0i} or n_{0i} , and $T_{0i}(r_0) = 1.97\text{keV}$, $n_{0i} = 10^{19}\text{m}^{-3}$, $\Delta_A = 0.30$, $\kappa_n \equiv R_0/L_n = 2.23$, $\kappa_T = 6.96$. L_n and L_T are the scale length of density and ion temperature, respectively. Here, $\tau_e = 1$ is assumed. A comparison of linear ITG frequency and growth rate between different codes are shown in Fig. B.8. The dimensionless number $k_\theta \rho_i$ is used to represent the toroidal mode number, where k_θ is defined by $k_\theta = nq_0/r_0$. There are good agreements between simulation results of two codes.

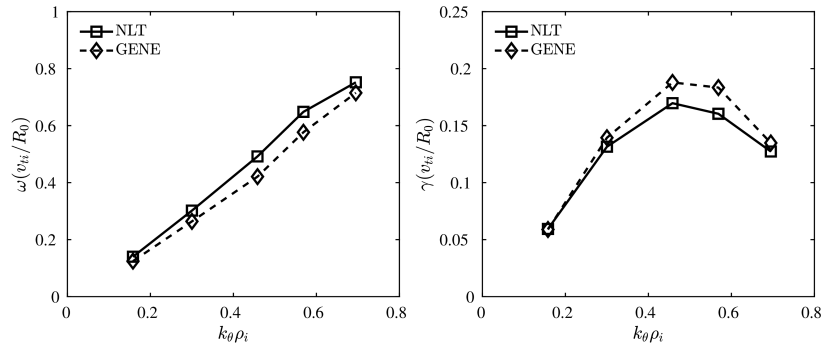


Figure B.8: Comparison of linear ITG frequency (a) and growth rate (b) between GENE and NLT.

Appendix C. Coefficients in the discretized $n = 0$ GK quasi-neutrality equation

The coefficient $\alpha_{j,k}^{j',k'}$, with $j \geq 2$, is given by

$$\alpha_{j,k}^{j',k'} = \begin{cases} \frac{1}{4}\Lambda_{r\theta}^{j+\frac{1}{2},k} + \frac{1}{4}\Lambda_{\theta r}^{j,k+\frac{1}{2}}, & j' = j+1, k' = k+1, \\ \frac{\Delta\theta}{\Delta r}\Lambda_{rr}^{j+\frac{1}{2},k} + \frac{1}{4}\Lambda_{\theta r}^{j,k+\frac{1}{2}} - \frac{1}{4}\Lambda_{\theta r}^{j,k-\frac{1}{2}}, & j' = j+1, k' = k, \\ -\frac{1}{4}\Lambda_{r\theta}^{j+\frac{1}{2},k} - \frac{1}{4}\Lambda_{\theta r}^{j,k-\frac{1}{2}}, & j' = j+1, k' = k-1, \\ \frac{1}{4}\Lambda_{r\theta}^{j+\frac{1}{2},k} - \frac{1}{4}\Lambda_{r\theta}^{j-\frac{1}{2},k} + \frac{\Delta r}{\Delta\theta}\Lambda_{\theta\theta}^{j,k+\frac{1}{2}}, & j' = j, k' = k+1 \\ -\frac{\Delta\theta}{\Delta r}\Lambda_{rr}^{j+\frac{1}{2},k} - \frac{\Delta\theta}{\Delta r}\Lambda_{rr}^{j-\frac{1}{2},k} - \frac{\Delta r}{\Delta\theta}\Lambda_{\theta\theta}^{j,k+\frac{1}{2}} \\ -\frac{\Delta r}{\Delta\theta}\Lambda_{\theta\theta}^{j,k-\frac{1}{2}}, & j' = j, k' = k \\ -\frac{1}{4}\Lambda_{r\theta}^{j+\frac{1}{2},k} + \frac{1}{4}\Lambda_{r\theta}^{j-\frac{1}{2},k} + \frac{\Delta r}{\Delta\theta}\Lambda_{\theta\theta}^{j,k-\frac{1}{2}}, & j' = j, k' = k-1 \\ -\frac{1}{4}\Lambda_{r\theta}^{j-\frac{1}{2},k} - \frac{1}{4}\Lambda_{r\theta}^{j,k+\frac{1}{2}}, & j' = j-1, k' = k+1 \\ -\frac{\Delta\theta}{\Delta r}\Lambda_{rr}^{j-\frac{1}{2},k} - \frac{1}{4}\Lambda_{\theta r}^{j,k+\frac{1}{2}} + \frac{1}{4}\Lambda_{\theta r}^{j,k-\frac{1}{2}}, & j' = j-1, k' = k, \\ \frac{1}{4}\Lambda_{r\theta}^{j-\frac{1}{2},k} + \frac{1}{4}\Lambda_{\theta r}^{j,k-\frac{1}{2}}, & j' = j-1, k' = k-1, \end{cases} \quad (\text{C.1})$$

where $\Lambda_{ab}^{j,k}$ represents $[c_0 J_X g^{ab}]^{j,k}$ and $[\cdot]^{j,k}$ represents the value at the (r_j, θ_k) . Here, the metric coefficient g^{ab} is defined as

$$g^{ab} = \begin{cases} \nabla\theta \cdot \nabla\theta - \left(\frac{\partial_r \psi}{JB}\right)^2, & a = b = \theta \\ \nabla a \cdot \nabla b, & \text{else,} \end{cases} \quad (\text{C.2})$$

where ψ is the poloidal magnetic flux. The coefficient $\beta_{j,k}^{j,k}$, with $j \geq 2$, is given by

$$\beta_{j,k}^{j,k} = \Delta r \Delta\theta [c_1 J_X]^{j,k}. \quad (\text{C.3})$$

The coefficient $\nu_{j,k}^{j,k'}$, with $j \geq 2$, is given by

$$\nu_{j,k}^{j,k'} = \Delta r \Delta \theta [c_1 J_X]^{j,k} \frac{[J_X]^{j,k'}}{\sum_{k''=1}^{N_\theta} [J_X]^{j,k''}}, \quad k' = 1, 2, \dots, N_\theta. \quad (\text{C.4})$$

The coefficient $\sigma_{j,k}^{j,k}$, with $j \geq 2$, is given by

$$\sigma_{j,k}^{j,k} = \Delta r \Delta \theta e_i [J_X]^{j,k}. \quad (\text{C.5})$$

References

- [1] G. Constantinescu, S. Lele, A highly accurate technique for the treatment of flow equations at the polar axis in cylindrical coordinates using series expansions, *J. Comput. Phys.* 183 (2002) 165–186.
- [2] M. D. Griffin, E. Jones, J. D. Anderson, A computational fluid dynamic technique valid at the centerline for non-axisymmetric problems in cylindrical coordinates, *J. Comput. Phys.* 30 (1979) 352–360.
- [3] W. Huang, D. M. Sloan, Pole condition for singular problems: The pseudospectral approximation, *J. Comput. Phys.* 107 (1993) 254–261.
- [4] J. P. Boyd, *Chebyshev and Fourier Spectral Methods*, Springer Berlin, Heidelberg, 1989.
- [5] T. Matsushima, P. Marcus, A spectral method for polar coordinates, *J. Comput. Phys.* 120 (1995) 365–374.
- [6] W. Verkley, A spectral model for two-dimensional incompressible fluid flow in a circular basin, *J. Comput. Phys.* 136 (1997) 115–131.
- [7] B. Fornberg, A pseudospectral approach for polar and spherical geometries, *SIAM J. Sci. Comp.* 16 (1995) 1071–1081.
- [8] K. Mohseni, T. Colonius, Numerical treatment of polar coordinate singularities, *J. Comput. Phys.* 157 (2000) 787–795.
- [9] S. K. Lele, Compact finite difference schemes with spectral-like resolution, *J. Comput. Phys.* 103 (1992) 16–42.

- [10] S. Wang, Z. Wang, T. Wu, Self-organized evolution of the internal transport barrier in ion-temperature-gradient driven gyrokinetic turbulence, *Phys. Rev. Lett.* 132 (2024) 065106.
- [11] A. J. Brizard, T. S. Hahm, Foundations of nonlinear gyrokinetic theory, *Rev. Mod. Phys.* 79 (2007) 421–468.
- [12] W. W. Lee, Gyrokinetic approach in particle simulation, *Phys. Fluids* 26 (1983) 556–562.
- [13] Z. Lin, T. S. Hahm, W. W. Lee, W. M. Tang, R. B. White, Turbulent transport reduction by zonal flows: Massively parallel simulations, *Science* 281 (1998) 1835–1837.
- [14] J. Candy, R. Waltz, An eulerian gyrokinetic-maxwell solver, *J. Comput. Phys.* 186 (2003) 545–581.
- [15] V. Grandgirard, Y. Sarazin, X. Garbet, G. Dif-Pradalier, P. Ghendrih, N. Crouseilles, G. Latu, E. Sonnendrücker, N. Besse, P. Bertrand, GYSELA, a full-f global gyrokinetic Semi-Lagrangian code for ITG turbulence simulations, *AIP Conf. Proc.* 871 (2006) 100–111.
- [16] S. Jolliet, A. Bottino, P. Angelino, R. Hatzky, T. Tran, B. Mcmillan, O. Sauter, K. Appert, Y. Idomura, L. Villard, A global collisionless pic code in magnetic coordinates, *Comput. Phys. Comm.* 177 (2007) 409–425.
- [17] Y. Idomura, M. Ida, T. Kano, N. Aiba, S. Tokuda, Conservative global gyrokinetic toroidal full-f five-dimensional vlasov simulation, *Comput. Phys. Comm.* 179 (2008) 391–403.
- [18] K. Obrejan, K. Imadera, J. Li, Y. Kishimoto, Development of a global toroidal gyrokinetic vlasov code with new real space field solver, *Plasma Fusion Res.* 10 (2015) 3403042–3403042.
- [19] H. Feng, W. Zhang, Z. Lin, X. Zhufu, J. Xu, J. Cao, D. Li, Development of finite element field solver in gyrokinetic toroidal code, *Commun. Comput. Phys.* 24 (2018) 655–671.
- [20] L. Ye, Y. Xu, X. Xiao, Z. Dai, S. Wang, A gyrokinetic continuum code based on the numerical lie transform (NLT) method, *J. Comput. Phys.* 316 (2016) 180–192.

- [21] Y. Xu, L. Ye, Z. Dai, X. Xiao, S. Wang, Nonlinear gyrokinetic simulation of ion temperature gradient turbulence based on a numerical Lie-transform perturbation method, *Physics of Plasmas* 24 (2017) 082515.
- [22] S. Wang, Transport formulation of the gyrokinetic turbulence, *Physics of Plasmas* 19 (2012) 062504.
- [23] S. Wang, Nonlinear scattering term in the gyrokinetic Vlasov equation, *Phys. Plasmas* 20 (2013) 082312.
- [24] Z. Dai, Y. Xu, L. Ye, X. Xiao, S. Wang, Gyrokinetic simulation of its turbulence with toroidal geometry including the magnetic axis by using field-aligned coordinates, *Comput. Phys. Comm.* 242 (2019) 72–82.
- [25] H. R. Lewis, P. M. Bellan, Physical constraints on the coefficients of Fourier expansions in cylindrical coordinates, *J. Math. Phys.* 31 (1990) 2592–2596.
- [26] H. Eisen, W. Heinrichs, K. Witsch, Spectral collocation methods and polar coordinate singularities, *J. Comput. Phys.* 96 (1991) 241–257.
- [27] S. Wang, Zonal flows driven by the turbulent energy flux and the turbulent toroidal Reynolds stress in a magnetic fusion torus, *Phys. Plasmas* 24 (2017) 102508.
- [28] K. H. Burrell, M. E. Austin, C. M. Greenfield, L. L. Lao, B. W. Rice, G. M. Staebler, B. W. Stallard, Effects of velocity shear and magnetic shear in the formation of core transport barriers in the dIII-d tokamak, *Plasma Phys. Control. Fusion* 40 (1998) 1585.
- [29] F. Zonca, L. Chen, Radial structures and nonlinear excitation of geodesic acoustic modes, *Euro. Phys. Lett.* 83 (2008) 35001.
- [30] M. N. Rosenbluth, F. L. Hinton, Poloidal flow driven by ion-temperature-gradient turbulence in tokamaks, *Phys. Rev. Lett.* 80 (1998) 724–727.
- [31] H. Sugama, T.-H. Watanabe, Collisionless damping of geodesic acoustic modes, *J. Plasma Phys.* 72 (2006) 825–828.

- [32] H. Sugama, T.-H. Watanabe, Erratum: ‘collisionless damping of geodesic acoustic modes’ [j. plasma physics (2006) 72, 825], J. Plasma Phys. 74 (2008) 139 – 140.

- [33] A. M. Dimits, G. Bateman, M. A. Beer, B. I. Cohen, W. Dorland, G. W. Hammett, C. Kim, J. E. Kinsey, M. Kotschenreuther, A. H. Kritz, L. L. Lao, J. Mandrekas, W. M. Nevins, S. E. Parker, A. J. Redd, D. E. Shumaker, R. Sydora, J. Weiland, Comparisons and physics basis of tokamak transport models and turbulence simulations, Phys. Plasmas 7 (2000) 969–983.